UC Berkeley
UC Berkeley Previously Published Works

Title

Nanometre-resolved observation of electrochemical microenvironment formation at the nanoparticle—ligand interface

Permalink

Journal

ISSN

Authors

Shan, Yu
Zhao, Xiao
Fonseca Guzman, Maria
et al.

Publication Date

DOI

Copyright Information

Nanometer-resolved observation of electrochemical microenvironment formation at the nanoparticle-ligand interface

Authors List

Yu Shan[1,2, †], Xiao Zhao[1,3,†], Maria Fonseca Guzman[2,4,†], Asmita Jana[2,5], Shouping Chen[1,2], Sunmoon Yu[1,2], Ka Chon Ng[3], Inwhan Roh[2,4], Hao Chen[2], Virginia Altoe[6], Stephanie N. Gilbert Corder[5], Hans A. Bechtel[5], Jin Qian[2], Miquel B. Salmeron[1,2,3*] and Peidong Yang[1,2,4,7,*]

Affiliations

[1]Department of Materials Science and Engineering, University of California at Berkeley; Berkeley, California 94720, United States

[2]Chemical Sciences Division, Lawrence Berkeley National Laboratory; Berkeley, California, 94720, United States

[3]Materials Sciences Division, Lawrence Berkeley National Laboratory; Berkeley, California, 94720, United States

[4]Department of Chemistry, University of California at Berkeley; Berkeley, California 94720, United States

[5]Advanced Light Source, Lawrence Berkeley National Laboratory; Berkeley, California, 94720, United States

[6]Molecular Foundry, Lawrence Berkeley National Laboratory; Berkeley, California, 94720, United States

[7]Kavli Energy NanoScience Institute, Berkeley, CA 94720, USA.

†These authors contributed equally to this work.

*Corresponding author. Email: mbsalmeron@lbl.gov, p_yang@berkeley.edu

Abstract

1   The dynamic response of surface ligands on nanoparticles (NPs) to external stimuli critically determines the

2   functionality of NP-ligand systems. For example, in electrocatalysis, the collective dissociation of ligands from NP

3   surfaces can lead to the creation of a NP/ordered ligand interlayer (NOLI), a microenvironment that is highly active

4   and selective for CO_2 to CO conversion. However, the lack of *in situ* characterization techniques with high spatial

5   resolution hampers a comprehensive molecular-level understanding of the interlayer formation mechanism. Here, we

6   utilize *in situ* Infrared nanospectroscopy (nano-FTIR) and surface-enhanced Raman spectroscopy (SERS), unveiling an

7   electrochemical bias-induced consecutive bond cleavage mechanism of the surface ligands, leading to the NOLI

8   formation. This real-time molecular insight could inspire the design of confined localized fields in multiple catalytic

9   systems. Moreover, the demonstrated capability to capture nanometer-resolved dynamic molecular-scale events holds

10   promise for advancing controlled local molecular behavior to achieve desired functionalities across multiple research

11   domains in nanoscience.

Introduction

Inorganic NPs capped by organic ligands have found extensive scientific applications, ranging from nanomedicine [1,2] to optoelectronics [3,4] and catalysis [5,6]. While the introduction of ligands has traditionally aimed at providing precise control of the NP size, shape, and colloidal stability [7,8], recent research has increasingly emphasized the critical role of ligands under relevant operating conditions in determining specific NP functionalities and phenomena [9,10]. In response to external stimuli, such as temperature, magnetic/electric fields, light, or pH, ligands can undergo reorganization, degradation, exchange, and notably, detachment, as a result of bond cleavage between the ligands and the NP surface [9,11]. Controlled ligand dissociation in specific biological environments, for instance, dictates the precise delivery of drugs [12-14]. In optoelectronic applications, the detachment of ligands plays a crucial role in augmenting the efficiency of charge transport between neighboring NPs [15].

Similarly, in electrocatalysis, the detachment of ligands from nanocatalysts is generally requisite to expose active metal sites to reactants [16]. Due to the electric field variation caused by ligand dissociation, this process can also induce favorable non-covalent interactions surrounding active sites [17,18]. This phenomenon engenders the creation of an electrocatalytic microenvironment, which is pivotal in parallel to active sites, for steering a specific reaction pathway [19]. An exemplary system is the NP/ordered-ligand interlayer (NOLI), which relies on ligand dissociation to establish a favorable reaction pocket that supports the remarkably efficient conversion of CO_2 to CO with 100% selectivity [17]. Specifically, it is hypothesized that ligands dissociate from the Ag NP assembly under electrochemical conditions, followed by NP aggregation, resulting in a structurally ordered layer adjacent to the evolved NP surface, and featuring an aqueous interlayer confined between the ligands and Ag surface (Fig. 1a). Furthermore, cations within the electrolyte are inserted into the interlayer and lose part of their solvation shells. These desolvated cations stabilize key intermediates, thus promoting a boosted turnover of CO_2 to CO [17].

Despite the remarkable catalytic performance of NOLI, direct evidence substantiating the existence of this interlayer is lacking. Moreover, if it indeed exists, the mechanisms governing its formation remain largely unclear, obstructing a comprehensive molecular-level comprehension of the interactions within the interlayer that ultimately lead to its catalytic performance. These constraints significantly limit the potential use of controlled ligand behavior to rationally design the microenvironments tailored for desired electrochemical reactions. To understand the ligand behavior under electrochemical conditions and its localized impact, it is imperative to capture the real-time ligand configurations in response to the electrochemical bias. Furthermore, given the inherent heterogeneity and substantial restructuring of ligand-NP systems upon ligand detachment [10,20], a spatial mapping of this process with nanometer precision becomes indispensable. Although challenging and unreported thus far, a direct probe of ligand dynamics under electrochemical conditions, with prerequisite spatial resolution on the order of NP size and chemical sensitivity, assumes a crucial role in providing molecular-level insights for the future design of nanocatalysts.

In this study, we utilize *in situ* infrared nanospectroscopy (nano-FTIR), complemented by *in situ* surface enhanced Raman spectroscopy (SERS) and density functional theory (DFT) calculations, to monitor the ligands' dynamic behavior in response to the electrochemical potential of the Ag-NOLI system. Assisted by these vibrational spectroscopies, we unveil how the bias-induced dissociation of tetradecylphosphonic acid ligands instigates the development of an electrocatalytic interlayer, which is stable in close proximity to the Ag surface. As illustrated in Fig. 1b, with a gradual increase in cathodic bias, *in situ* nano-FTIR captures the transition from a bidentate to monodentate ligand binding configuration on the aggregating NPs. Additionally, SERS captures the transformation from monodentate to free ligands and the conformational change of the alkyl chains. This consecutive dissociation of ligands, further supported by DFT simulations, offers a real-time picture of how the bias and electrochemical environment modulate ligand-NP interactions. In addition, we also reveal the gradual buildup of the noncovalent interactions, mediated by the ligand dissociation process, among the Ag surface, detaching ligands, and electrolyte species. These interactions collectively contribute to the development of the confined electric field within the microenvironment, thereby promoting high catalytic performance.
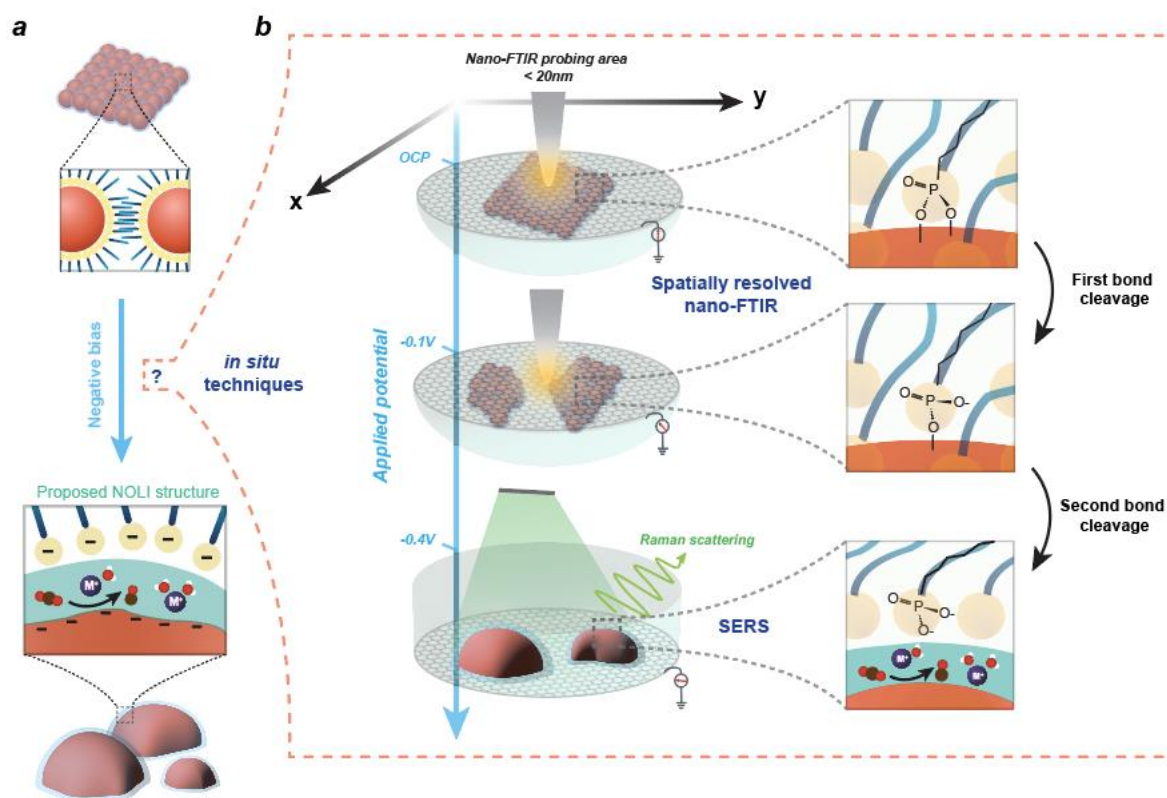
Fig. 1. Real-time molecular picture of microenvironment formation probed by *in situ* nano-FTIR and SERS. a, The proposed initial and final states during NOLI formation [17,18]. **b**, Probed NOLI formation mechanism. Under low overpotential, *in situ* nanometer-resolved nano-FTIR reveals the cleavage of one of the P-O-Ag bonds on the aggregating NPs. Meanwhile, the second P-O-Ag bond cleavage is observed by *in situ* SERS under high overpotentials. This combination uncovers a consecutive bond cleavage mechanism that promotes the formation of favorable

62 noncovalent interactions between CO_2, cations, solvent, and ligands, which are responsible for the high catalytic

63 activity of NOLI (C, brown; cation, purple; O, red; H, grey; ligand head group, yellow; ligand alkyl chains, blue;

64 aqueous interlayer, cyan).

Results

65 **Initial Binding Configuration of Ligands Probed by Nano-FTIR**

66 To investigate spatially inhomogeneous chemical processes *in situ* while minimizing radiation damage,

67 vibrational spectroscopy/spectromicroscopy techniques with low excitation energy, such as nano-FTIR, are preferable

68 [21-23]. In the experimental setup depicted in Fig. 2a, a broadband, spatially coherent synchrotron IR beam is focused onto

69 the metal-coated probe of an atomic force microscope (AFM). The sharp tip acts as an antenna that creates a large

70 enhancement of the IR field near the apex, which decays exponentially with distance, resulting in a high spatial

71 resolution (typically < 20 nm) with surface and chemical sensitivity [21,23]. Furthermore, due to the approximate alignment

72 of the IR near field with the axis of the AFM probe, vibrational modes with dipoles along the same direction are

73 selectively excited. This polarization facilitates the detection of molecular orientation, which can be characterized by

74 changes in the relative peak intensities of vibrational modes [21,24,25]. The recent development of liquid cells with single

75 layer graphene windows that are transparent to photons has facilitated the utilization of nano-FTIR for studying

76 organic molecules under electrochemical conditions [26-29]. In the current experimental configuration, the detection under

77 CO_2 reducing condition and the replication of Ag NP evolution (Fig. 2b, c) is achieved, demonstrating the suitability of

78 this platform for investigating the formation of NOLI *in situ*.

79 To study the initial binding configuration of ligands, the as-prepared Ag NPs are assembled on the single-

80 layer graphene facing the electrolyte (Fig. 2a, b). The corresponding nano-FTIR spectrum under open circuit potential

81 (OCP) is shown in Fig. 2d, revealing multiple peaks around the P-O stretch region that are the IR fingerprint of the

82 tetradecylphosphonic acid (TDPA) ligand used in the synthesis of the NPs (Supplementary Figure 1). From DFT

83 calculations (Supplementary Table 1, Supplementary Note 1) and previous studies [30-34], the peak around 1039 cm^{-1} can

84 be assigned to the symmetric stretch of P-O (ν_s(P-O)), and the peaks around 1112 cm^{-1} and 1170 cm^{-1} to the asymmetric

85 stretch of P-O (ν_{as}(P-O)) coupled with C-C stretch (ν(C-C)) and with C-H twisting (τ(C-H)), respectively. For simplicity,

86 ν_{as}(P-O) will be used to refer to these two asymmetric modes in the following discussion, while ν_s(P-O) specifically

87 refers to the mode at 1039 cm^{-1}. In addition, the mode at 1305 cm^{-1} belongs to the P=O stretch (ν(P=O)) [31]. The orthogonal

88 vibrations of ν_s(P-O) and ν_{as} (P-O) are particularly sensitive to the polarization of the IR radiation, which can provide

89 valuable insights into the initial binding structure of the ligand on the Ag surface [35]. Based on the dominant intensities

90 of the ν_s(P-O) mode in the P-O stretch region and the presence of the ν(P=O) mode, it can be concluded that TDPA

91 binds to the Ag surface through a bidentate mode when immersed in the electrolyte. As illustrated in the schematic

92 representation of the modes in Fig. 2d, a bidentate binding structure allows for a dipole moment of the ν_s(P-O) mode

93 along the surface normal, leading to a high nano-FTIR intensity. Under the same configuration, the ν_{as} (P-O) mode,

94 which has a dipole moment parallel to the surface, exhibits a low intensity. This non-zero intensity comes from the

95 orientation variation of the ligand on the NP surface with large curvature, allowing some coupling with the near field.
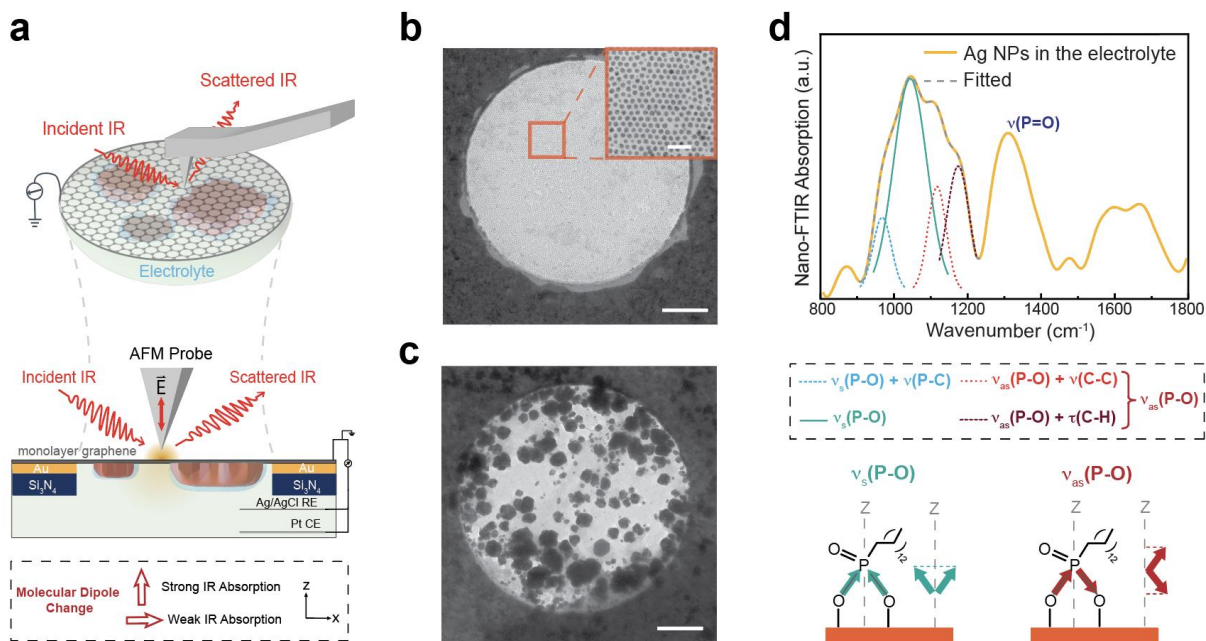
Fig. 2. *In situ n*ano-FTIR setup and determination of initial binding configuration of ligands on Ag NPs. **a**, A schematic of the nano-FTIR experiment. The AFM probe is located over one of the graphene windows suspended across the holes of a perforated 100 nm thick Si_3N_4 membrane (the diameter of the hole is 1 μm and only one hole is shown in this schematic). The single-layer free-standing graphene closing the cell serves both as the working electrode and as the separation between the aqueous environment and the AFM tip, thus preventing tip damage and contamination [27,28]. The cell is filled with 0.1 M $KHCO_3$ solution saturated with CO_2 and the entire setup is situated in a dry N_2 environment. **b-c,** *Ex situ* transmission electron microscopy (TEM) images of the monolayer Ag NPs drop cast onto the graphene facing the electrolyte (**b**), and their evolved state after the application of negative bias (**c**). The scale bar is 100 nm in b and c. The inset in b shows the densely packed monolayer particles, with a scale bar of 25 nm. **d,** Nano-FTIR spectrum of Ag NPs inside the cell filled with electrolyte under open circuit condition. The P-O stretch region is composed of four different modes around 962 cm^{-1} (blue, dotted), 1039 cm^{-1} (cyan), 1112 cm^{-1} (red, dotted), and 1170 cm^{-1} (brown, dotted), which correspond to ν_s (P-O) coupled with ν (P-C), ν_s (P-O), ν_{as} (P-O) coupled with ν (C-C), and ν_{as} (P-O) coupled with τ (C-H), respectively. Schematics of the relative movement of atoms in symmetric and asymmetric modes, as well as the corresponding dipole change projected along the z direction (surface normal) are depicted below the spectrum.

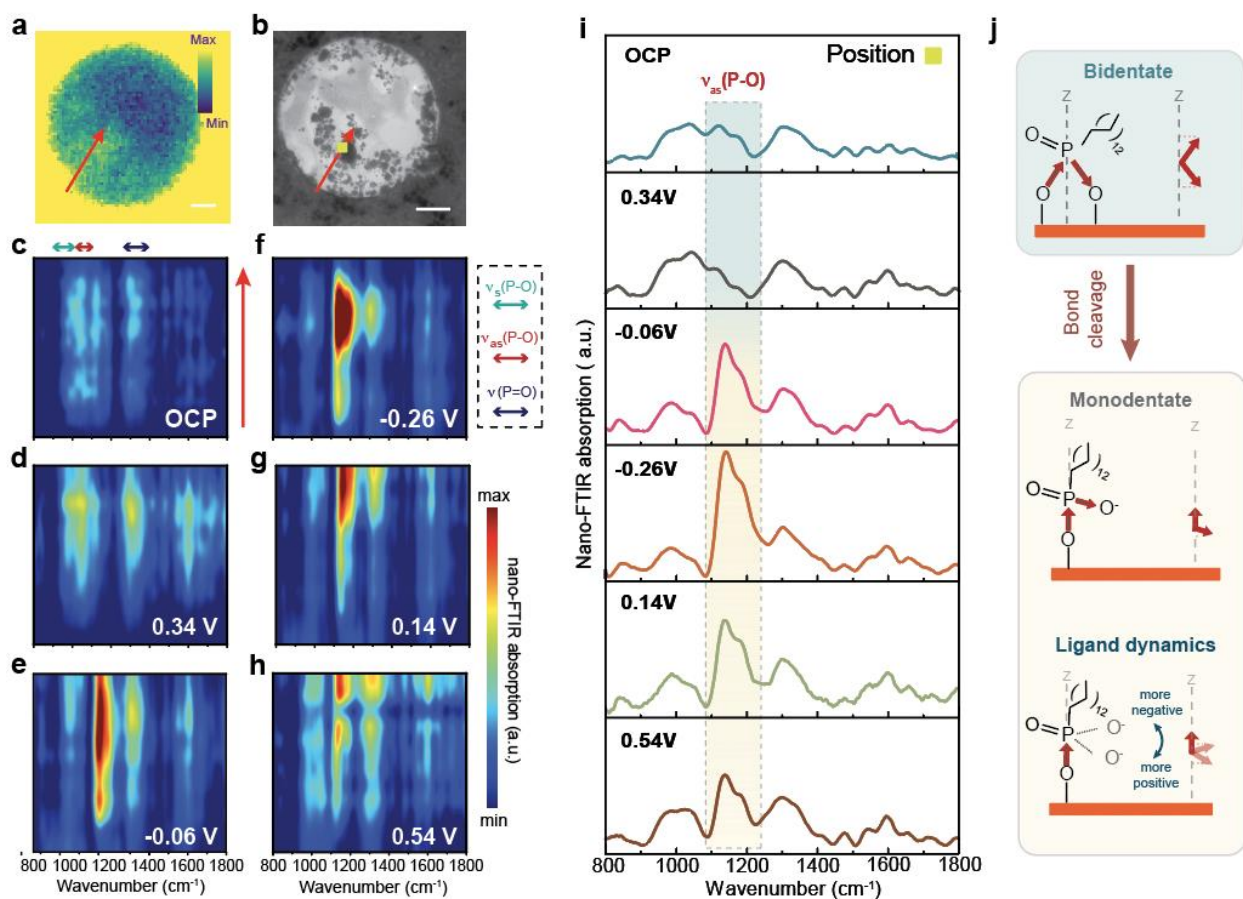**Bias-Induced Bidentate to Monodentate Transformation**

112   The structural evolution of ligands on the Ag NPs is revealed by the nano-FTIR line profiles captured under

113 electrochemical conditions (Fig. 3). Fig. 3a displays the image of the integrated near-field IR amplitude scattered from

114 the tip-sample region during scanning over the graphene-covered window and surrounding regions. The

115   corresponding transmission electron microscopy (TEM) image of the same area, acquired after the nano-FTIR

116   experiment, reveals the NP distribution of the evolved state (Fig. 3b). While the near-field IR image exhibits a somewhat

117   lower spatial resolution compared to the TEM image, we employ it for localizing the aggregation of nanoparticles

118   during the nano-FTIR experiment. To preserve the integrity and functionality of the TDPA ligand, samples were not

119   exposed to electron beam prior to the nano-FTIR experiments, considering the extreme sensitivity of organic ligands

120   to electron beam radiation [36,37].

121   Nano-FTIR line profiles under different biases, acquired along the scan direction represented by a red arrow

122   (Fig. 3a, b), are visualized as 3D color maps depicting line scans over which the intensity of nano-FTIR absorption is

123   recorded (Fig. 3c-h). All biasing potentials in this work are referenced to the reversible hydrogen electrode (RHE),

124   unless indicated otherwise. At OCP, which is approximately 0.71 V at pH 6.8, the intensity distribution of three P-O

125   stretch modes (ν_s(P-O), ν_{as}(P-O), ν(P=O)) of the phosphonate head group indicates a relatively homogeneous

126   distribution of the as-prepared NPs within the graphene window. When a bias of 0.34 V is applied, the nano-FTIR line

127   profile (Fig. 3d) shows some spatial inhomogeneities, which we attribute to the initial rearrangement of ligands.

128   Interestingly, at -0.06 V, a boost in intensity of the ν_{as}(P-O) mode is observed, while the spatial inhomogeneity remains

129   similar. At -0.26 V, when the NPs are expected to begin fusing together (Supplementary Figure 2), the IR line profile

130   becomes highly inhomogeneous, characterized by the augmented localization of the intensity of the ν_{as}(P-O) mode

131   (Fig. 3f). Careful comparison between the IR line profile and the TEM image confirms that NPs aggregate and fuse

132   together at positions where the concentrated IR intensity is observed. Upon reduction of the bias, a decay of the ν_{as}(P-

133   O) mode intensity is observed. To better present the bias-induced intensity change of the ν_{as}(P-O) mode, nano-FTIR

134   spectra taken in a representative position are provided in Fig. 3i.

135   The observed changes in the intensities of the ν_{as}(P-O) mode can be attributed to corresponding structural

136   modifications of TDPA ligands. At a bias of -0.06 V, we propose that the enhanced intensity of the ν_{as}(P-O) mode is

137   attributed to the partial dissociation of Ag-O bonds, indicating a transition from bidentate to monodentate binding

138   configuration of the ligand head group. This structural transformation accounts for the boost in the intensity of ν_{as}(P-

139   O) mode in two ways. Firstly, this transformation releases one O atom with partial negative charges from the surface,

140   drastically augmenting the overall dipole moment of the ν_{as}(P-O) mode. Secondly, as depicted in Fig. 3j, the lifted O

141   atom reorients the ligand structure, increasing the dipole moment projection of ν_{as}(P-O) mode along the surface

142   normal direction. It is crucial to highlight that alternative factors that might account for the augmented intensity of the

143   ν_{as}(P-O) mode, such as Localized Surface Plasmon Resonance (LSPR) or an increased concentration of ligands, can be

144   discounted. This is because if these factors were the primary drivers, one would expect a uniform increase in intensity

145   across a broad wavenumber range. However, we only observe the increased intensity exclusively in the ν_{as}(P-O) mode.

146   Once the monodentate configuration is formed, the electrostatic interaction between the detached O atom and

147   the negatively charged Ag surface dictates a highly sensitive and dynamic response of the ligand structure to the

148   applied bias. Under -0.26 V, the boosted intensity of ν_{as}(P-O) indicates that the ligand structure remains in the

149   monodentate configuration, which is further supported by the remaining P-O-Ag covalent interaction observed by X-

150   ray photoelectron spectroscopy (XPS) (Supplementary Figure 7-8). However, a greater accumulation of surface charge

151   compared to that under -0.06 V results in a larger separation between the detached O atoms and the Ag surface driven

152   by repulsion. This separation decreases upon gradual retraction of the bias (decrease of the overpotential), explaining

153   the decrease in the intensity of the ν_{as}(P-O) mode when we retract the bias to 0.14 V and 0.54 V, as illustrated in Fig.

154   3g-h and Fig. 3i.

155   **Fig. 3. Spatially resolved bidentate to monodentate transformation and structural dynamics. a,** Images of the total

156   scattered optical amplitude from the suspended graphene with NPs and its surrounding area. The intensity increases

157   when the tip is positioned on the top of the region outside the suspended graphene window because the gold film

158   under the graphene scatters more IR light (scale bar, 100 nm). **b,** Corresponding TEM image of the same area after the

159   nano-FTIR experiment (scale bar, 100nm). **c-h,** Color map representations of the nano-FTIR spectral intensities

160   (arbitrary units in the color scale) from 800 to 1800 cm^{-1} over the Ag NPs under various biases. The ranges for stretching

161   modes of P-O and P=O are indicated. The nano-FTIR profiles were acquired at positions along the red arrows in **a** and

162   **b**. The electrochemical bias was applied in the following manner: OCP→ 0.34 V→ -0.06 V→ -0.26 V→ 0.14 V→ 0.54 V.

163   Each nano-FTIR spectra is collected under a constant potential in 0.1 M KHCO₃ (pH 6.8) saturated with 1 atm CO₂. **i,**

164   Stacked nano-FTIR spectra (left panel) under stepped bias collected at the position on the line scan marked by a soft
165   green square in **b**. **j,** The mechanism of intensity variations of the ν_{as}(P-O) mode under different potentials. All the
166   potentials in this figure are referenced to the reversible hydrogen electrode (RHE).

167   **Microenvironment Formed by Transformation to Free Ligand**

168   　　　　The *in situ* nano-FTIR measurement captures the bias-induced bond cleavage and structural dynamics of the
169   ligands. The high spatial resolution uniquely allows a direct comparison of spectra originating from NPs of varying
170   sizes and evolving statuses, which leads to the conclusion that the bidentate to monodentate transformation occurs
171   universally across all NP surfaces, maintaining consistent ligand structural dynamics irrespective of NP sizes
172   (Supplementary Note 2). However, within the bias window stabilizing the monodentate configuration, no evidence
173   suggests the occurrence of CO_2 reduction, and the current nano-FTIR/graphene cell setup suffers from the fragility of
174   the graphene membrane under greater bias (beyond -0.26 V). To circumvent this problem and to capture the final
175   ligand state supporting CO_2 reduction, we use surface enhanced Raman (SERS) to follow the evolution of the molecular
176   structure within NOLI up to more negative bias compared to those currently possible with nano-FTIR. This enables
177   tracking changes of ligand species through the onset of full detachment. The Raman scattering experiments employ a
178   focused laser beam that passes through the electrolyte and is focused on the electrode surface (Fig. 4a**).** However, SERS
179   is not polarized and hence there is no preferential orientation axis like in nano-FTIR.

180   　　　　The initial state of the ligand on Ag NPs (Fig. 4b), in electrolyte, is characterized by three main Raman peaks
181   at 540 cm^{-1}, 711 cm^{-1}, and 780 cm^{-1} within the spectral range between 400 and 900 cm^{-1} (Fig. 4b). The peak at 540 cm^{-1} is
182   assigned to O-P-O wagging (out-of-plane bending) mode of the ligand head group bound to Ag surface, supporting a
183   bidentate ligand configuration on the as-prepared NPs (Supplementary Table 1). The C-P stretching mode is located at
184   780 cm^{-1}, with a shoulder peak at 711 cm^{-1} which is assigned to alkyl C-C bending [31-33]. Upon initial biasing, the O-P-O
185   wagging mode disappears. As predicted and shown in other works, this type of mode can be highly dependent on the
186   binding configuration and even surface geometry, given that the prominent structural change due to the detachment
187   of an O atom can contribute to distinct active modes, supporting that a change in ligand configuration is occurring
188   upon initial biasing [31,32,34]. Meanwhile, the continued appearance of C-P stretches confirms the ligand is still detectable
189   near the surface. Together, this compellingly demonstrates the detachment of first Ag-O bonds and supports the results
190   from nano-FTIR (Supplementary Note 5).

191   　　　　Under the same conditions, a dominant peak emerges at 530 cm^{-1}, which belongs to the P-O bending modes
192   (i.e., $\boldsymbol{\delta}$(O-P-O), or $\boldsymbol{\delta}$(C-PO$_3$)) [34,38]. This mode exhibits a red shift of 10 cm^{-1} compared with the wagging mode of the
193   initial state, which arises from a distinct ligand configuration following the second Ag-O detachment occurring
194   between -0.40 and -0.65 V [31-33]. Under higher bias (-0.40 V and greater, Fig. 4b), the sharp peak at 710 cm^{-1} is assigned to
195   CO_3^{2-} bending mode and accompanied by the depletion of the bicarbonate CO-H mode (1042 cm^{-1}). This confirms a
196   change in the pH near the surface that occurs at the onset of CO_2 reduction in the NOLI, in agreement with the onset

197 of Faradaic currents observed by linear sweep voltammetry (LSV) (Fig. 4d). As expected, the second detachment

198 prompts interlayer formation, causing substantial changes within the local electrochemical environment, and the onset

199 of efficient CO_2 reduction marked by a change in the reactive species present [17].

200 Utilizing the C-H$_x$ region, containing asymmetric and symmetric stretching modes (2800 – 3000 cm^{-1}), the bias-

201 induced behavior of the alkyl chains is captured. A peak at 2821 cm^{-1} emerges starting from - 0.40 V (Fig. 4c), which

202 remains unreported in many spectroscopic studies focused on alkyl chains and their assemblies [39-41]. Notably, this peak

203 is negligible during the bias-induced detachment process of a TDPA assembly on polished (planar) Ag foil

204 (Supplementary Figure 16), which offers a contrast to the ligand behavior arising from surface curvature-induced

205 ligand-ligand interactions which can be stabilized under biasing conditions in NOLI[18]. Furthermore, the bias-

206 dependent behavior of this mode is reversible, as the peak disappears when the bias is retracted (Fig. 4c). Based on

207 these observations, we propose this peak represents a C-H stretching mode which originates from the presence of

208 solvent molecules situated between alkyl chains. This proposition stems from the understanding that while the ligand

209 layer remains in proximity to the NP after detachment, applying greater bias expands the spatial region that an

210 individual ligand can explore as it is electrostatically repelled from the surface. This process increases the likelihood of

211 water intercalation between the ligand chains and these water molecules would potentially weaken the C-H stretch

212 mode (Supplementary Figure 16, Supplementary Note 6).
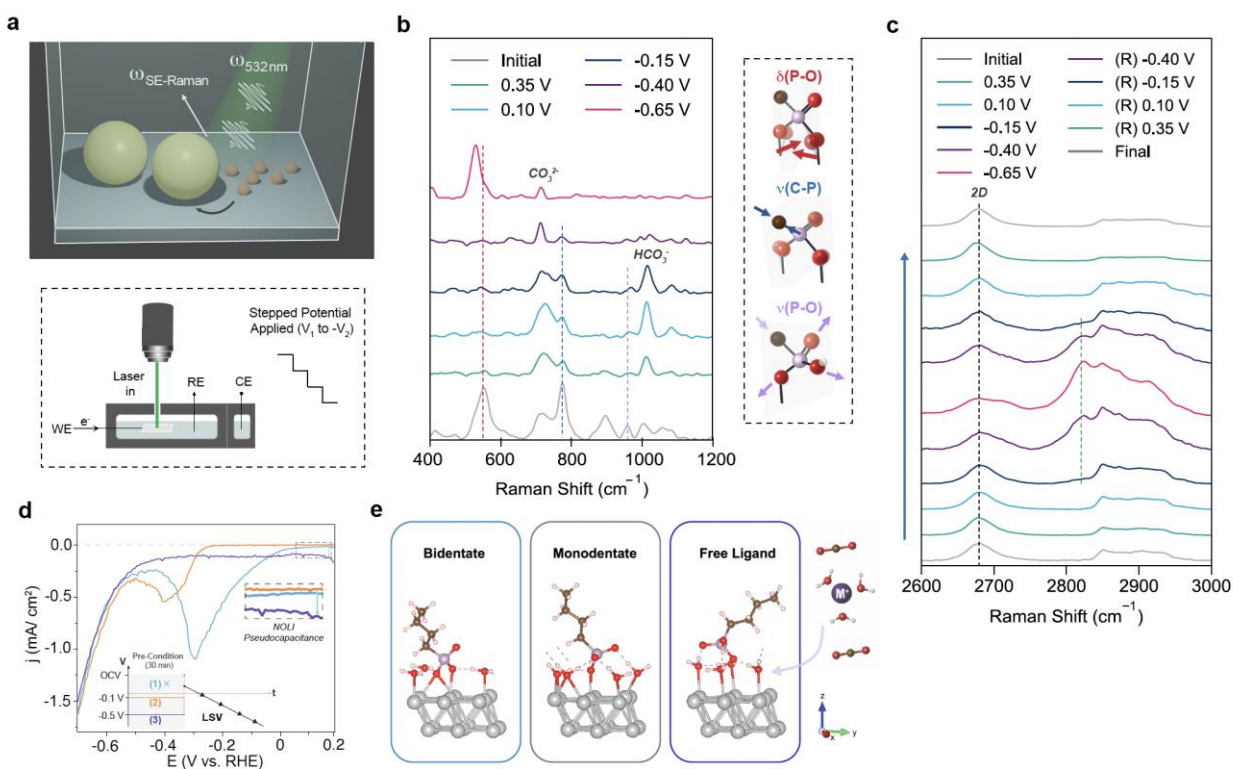
213 **Fig. 4. Bias-induced second bond cleavage towards formation of the catalytic interlayer**. **a,** Simplified schematic of

214 *in situ* Raman spectro-electrochemical set-up conducted in a customized cell. A roughened Ag substrate is used to

215 further boost scattering enhancement and one layer of graphene is transferred onto the surface. Ag NPs are then drop
216 casted onto graphene capped electrodes. **b,** *in situ* Raman spectra from the Ag NPs on the graphene/SERS electrode in
217 0.1 M KHCO$_3$ (pH 6.8). Illustrations show O-P-O wagging, C-P stretching, and P-O symmetric stretching modes with
218 the C$_{14}$ alkyl chain represented for simplicity by one C atom (brown). Each of these modes is indicated by a dashed line
219 in the left spectra. The remaining peaks at 1007 and 1064 cm^{-1} are assigned to bicarbonate CO-H bend and carbonate
220 symmetric stretching modes, respectively, and carbonate bending at 710 cm^{-1}, from the electrolyte [42]. **c,** *in situ* Raman
221 spectra in the C-H$_x$ region. In the range of 2850 and 2950 cm^{-1}, methylene (-CH$_2$) and methyl (-CH$_3$) symmetric and
222 asymmetric stretches appear. The peak at 2825 cm^{-1} appears at greater applied biasing conditions (green dashed line).
223 The presence of a high-quality layer of graphene is confirmed by the presence of graphene's 2D mode around 2680 cm^{-}
224 ^{1} (Supplementary Figure 14) [43]. All Raman peak intensities are normalized to this mode. Potentials in **b** and **c** are
225 referenced to the reversible hydrogen electrode (RHE). **d,** LSV from 0.2 V to -0.7 V of as-prepared Ag NPs without
226 holding (blue) and after holding at -0.1 V (orange), or -0.5 V (purple) for 30 mins. **e,** Optimized structures obtained
227 through DFT calculations (0 V vs. Standard Hydrogen Electrode).

228   The bias-induced step-by-step detachment mechanism of the ligand can be further supported by a careful
229 analysis of the LSV. As shown in Fig. 4d, after a cathodic scan from 0.2 V up to -0.7 V, a broad cathodic peak is observed,
230 which is due to the elimination of covalent interactions between ligands and NPs (blue curve) [17]. However, when the
231 NPs are preconditioned at a constant potential of -0.1 V for 30 min, the subsequent LSV scan distinctly shows a cathodic
232 peak centered around -0.4 V (orange curve). This indicates the broad cathodic peak of the blue curve contains at least
233 two sequential differentiated charge transfer processes with onset potentials corresponding to 0.1 V and -0.3 V. These
234 two sequential processes can be assigned as first and second Ag-O bonds cleavage (Supplementary Figure 8), respectively,
235 which aligns well with the observations in nano-FTIR and SERS experiments. Interestingly, the LSV scan after
236 preconditioning at -0.5 V (both bonds are dissociated) exhibits a nonzero non-Faradaic current from 0.2 V to -0.2 V
237 (purple curve), in contrast to the zero current observed after being held at -0.1 V (orange curve). This observation
238 supports that the insertion of charged species (i.e. K$^+$) to the ligand-Ag interface can only occur after both Ag-O bonds
239 are dissociated. Furthermore, no notable difference in selectivity and activity between direct and stepped potential
240 application has been observed for NOLI. This indicates that stepping of the applied potentials used in nano-FTIR, SERS,
241 and LSV experiments does not interfere with the formation of the NOLI structure (Supplementary Figure 17).

242   To gain more detailed insights into the ligand dissociation mechanism, DFT calculations are performed, which
243 provide an additional support for the initial state of a bidentate structure under OCP (Fig. 4e, Supplementary Method).
244 The calculations also reveal that the presence of intercalated water molecules on the Ag surface, evidenced by sum
245 frequency vibrational spectroscopy (SFVS) (Supplementary Figure 18, Supplementary Note 7), was essential for the
246 stability of the detaching ligands (Supplementary Figure 20). Furthermore, as indicated by the calculated energetic
247 phase diagram (Supplementary Figure 21), a more negative bias amplifies the electrostatic repulsion between the
248 negatively charged surface and the ligand head group, which serves as the driving force of the bond cleavage. The
249 complete detachment of ligands not only provides the space for cation insertion (Fig. 4c-d), but the resulting negatively
250 charged layers (both the charged Ag surface and the detached ligand head groups are negatively charged) promote

251 the partial shedding of the cations' solvation shell, thereby exposing positive charges to stabilize the NOLI structure [17].

252 This partially solvated cation has been shown to play a crucial role in enhancing the electron transfer in electrocatalytic

253 systems [44,45].

Conclusion

255   In this study, we employ a suite of *in situ* spectroscopic techniques and elucidate the formation pathway of a

256 microenvironment through bias-induced ligand detachment at the nanometer scale. By unraveling the molecular-scale

257 events that accompany this process, we gain a comprehensive understanding of the evolution of electric field confined

258 near the NP surface, mediated by ligand dynamics, which supports favorable non-covalent interactions and thus

259 enhances the selectivity and activity. These insights offer fundamental knowledge for guiding the design of

260 electrocatalysts through traceable structural evolution of the NP-ligand systems. Furthermore, the methodology

261 presented in this work could be universally applied to investigate the dynamic response of various interfacial species

262 (capping ligands, reaction intermediates, solvent molecules) to multiple external stimuli and with nanometer spatial

263 resolution, thereby substantially facilitating the mechanistic understanding of how the molecular-level events

264 ultimately leads to specific NP functionalities and phenomena. This holds great importance for providing fundamental

265 guiding principles for the rational design of responsive ligand-NP systems of desired functionalities with precise

266 dosage-, spatial- and temporal- control across medicine, optoelectronics, and energy fields.

Methods

268

NP synthesis and Ag foil preparation

270   Ag NPs were synthesized following the previously reported procedures [17]. For TDPA assembled Ag foil (Alfa

271 Aesar, 99.9%), Ag foil was initially mechanically polished using 2000G sandpaper, followed by Alpha alumina powder

272 with decreasing sizes of 1, 0.3, and 0.05 micrometers until achieving mirror shiny. The polished Ag foil was immersed

273 in 10 mM TDPA ethanolic solution overnight, and adequately rinsed with ethanol and deionized water.

Electrochemical measurement

275   All the electrochemical measurements were conducted using a customized H-cell, with an anion exchange

276 membrane (Selemion, AMV) separating working and counter chambers. The reference electrode was Ag/AgCl 3 M KCl

277 (World Precision Instruments), and the counter electrode was an electropolished platinum wire. The conversion of

278 electrode potentials from Ag/AgCl 3 M KCl to the reversible hydrogen electrode (RHE) is achieved through: E (vs.

279 RHE) = E (vs. Ag/AgCl 3 M KCl) + 0.210 + 0.0591 × pH. In terms of electrochemical testing, a stepped potential program

280 was employed using the chronoamperometry (CA) technique with two continuous biases. A scan rate of 50 mV/s was

281 used in the Linear sweep voltammetry (LSV) and cyclic voltammetry (CV) and 85% of the ohmic losses were

282 compensated automatically by the potentiostat (Biologic), while the remaining 15% was manually post-corrected. In

283 terms of catalyst loading, 29 μg of Ag NPs were deposited on the 1 cm² carbon paper (29AA). To remove the ligand

284 layer from the Ag-NOLI electrode, the electrode was biased under -1.3V vs. Ag/AgCl for 20 min and rinsed thoroughly

285 with 1 M KOH. We used Scanning electron microscopy (SEM) to confirm the intactness of the particles.

286 *nano-FTIR measurements*

287 Nano-FTIR measurements were conducted at beamline 2.4 and 5.4 of the Advanced Light Source at the

288 Lawrence Berkeley National Laboratory. The details of graphene membrane fabrication and the graphene liquid cell

289 have been previously reported [27,28]. Following the graphene transfer process, a hexane suspension containing 2 μg of

290 NPs was drop-casted onto the corrugated side of the graphene membrane. The details of the experimental setup and

291 data analysis process can be found in the published work[28].

292 *Preparation of Raman measurements*

293 Samples for *in situ* Raman experiments were prepared starting from an anodized Ag foil. The foil was then

294 treated via the reported method for roughening of Ag for purposes of boosting SERS performance. First, Ag foil was

295 gently sanded down and electrodes were cut to a desired size. Ag electrodes were then sonicated in Milli-Q water (18.2

296 MΩ) to remove any loose Ag remaining on the surface. Electrodes are then submerged in a 30% NH_4OH solution for

297 45 seconds and rinsed with Milli-Q water, followed by submersion in 6 M HNO_3 for 90 seconds[46]. After, electrodes are

298 rinsed, sonicated, and treated in an oven at 60 ºC. Prior to graphene transfer, Ag-roughened electrodes are treated with

299 plasma for 1 min to remove surface impurities. Graphene transfer is conducted in the same manner as described for

300 Nano-FTIR membranes. Electrodes are annealed overnight to improve the stability of graphene under aqueous

301 environment and biasing prior to use. Ag NPs are deposited on the graphene-capped Ag roughened (g-SERS)

302 electrodes. For control measurements of HPO_4^{2-}/PO_4^{3-}, a liquid sample holder was used, the solution was transferred

303 onto the g-SERS electrodes for Raman measurements.

304

305 *Electrochemical Raman spectroscopic measurements*

306 *In situ* measurements were performed in a custom-built Raman spectro-electrochemical cell with the working

307 electrode consisting of the 6 nm Ag NPs deposited on chemically roughened Ag surface, Ag/AgCl 3M KCl reference

308 electrode (World Precision Instruments), and Pt mesh counter electrode. The ohmic drop (ZIR) of the electrochemical

309 cell was compensated for each spectrum and chronoamperometry (CA) was run by stepping subsequently towards

310 more negative potentials using a Biologic potentiostat. Raman spectroscopic measurements were obtained using the

311 Horiba LabRAM HR Evolution. Excitation at 532 nm from an HeNe laser source which was focused through a 20x

312 microscope objective (Olympus). The incident laser to the system was attenuated by a D 0 - 0.3 filter (6~8mW/μm^2).

313 The hole size was 200 μm and the focus plane of electrode samples was focused using white light from a halogen lamp

314 or directly via laser illumination. In addition, the Raman spectrometer was equipped with a diffraction grating of 600

315 gr/mm. This was a preferred choice of grating as it ensured adequate signal acquisition even from samples covered by

316 a thick layer (several millimeters) of aqueous electrolyte. Collection parameters were set at 10 s exposure, 30 s RTD

317 exposure, and 5 s for potentiostatic measurements at negative applied potentials (V) in Fig. 4 (main text), or 10 s for

318 measurement of powder TDPA Raman spectra used in Supplementary Figure 10. The background of Raman spectra

319 was removed via LabSpec 5 software, and a Savitzky-Golay smoothing method (parameters set to 31, 6) was applied.

320 *Density Functional Theory calculation*

321 Density functional theory (DFT) calculations were employed using Vienna Ab initio Simulation Package

322 (VASP) [47-49] to obtain the optimized structures of the ligand on the Ag surface in various configurations: tridentate,

323 bidentate, monodentate, and non-dentate, consisting of 3, 2, 1, and 0 O atoms of the ligand, respectively, attached to

324 the surface. The projector augmented wave (PAW) method [50] was employed, and the generalized gradient

325 approximation(GGA) was used to describe the exchange-correlation [51]. To account for van der Waals (vdW) forces, the

326 D3 correction method of Grimme et al [52] was incorporated. We used an energy cutoff of 550 eV for all systems. K-points

327 meshes of 11x11x11 and 1x1x1 were used for bulk Ag and ligand in vacuum, respectively, while a 7x7x1 mesh was

328 used for surface calculations. We used the Ag (111) surface for our calculations because it is the most stable Ag surface[53].

329 To simulate the experimental ligand coverage of 1 ligand in 29 $Å^2$ of Ag surface, a 2x2 supercell (with an edge length

330 of 5.9 Å) in the x-y plane with one ligand was chosen as the model structure. Of the six silver atomic layers, the bottom

331 three were kept fixed while the top three layers were allowed to move during the relaxation. An additional 15 Å of

332 vacuum was imposed in the z direction to prevent undesirable neighboring interactions (Supplementary Figure 19).

333 The computational setup used is described in more detail in Supplementary Method. While the ligand used in the

334 work contains 14 carbon atoms (($CH_2)_{13}CH_3$) attached to a phosphonic head group, a 4-carbon atom chain-based

335 (($CH_2)_3CH_3$) ligand is considered sufficient to capture the binding configuration to minimize the calculation cost

336 (Supplementary Table 7). All the geometry relaxations were converged to within 10^{-5} eV of the total energy. For surface

337 relaxations, it was found advantageous to relax the structure in stages: a rough relaxation to 10^{-4} eV was followed by a

338 refined relaxation to 10^{-6} eV of the total electronic energy. The net charge of the system was set to -2 for the tridentate,

339 bidentate, and monodentate configurations while the non-dentate with one attached H had a net charge of -1.

340 *Sum frequency vibrational spectroscopy measurement*

341 We use the same SFVS experimental setup as in our previous papers[54].

342 *Structural characterization of NPs*

343 The sizes and shapes of the as-prepared NPs were checked by transmission electron microscopy (Hitachi H-

344 7650) while the evolving status on carbon paper was characterized by Scanning electron microscopy (Ultra 55-FESEM).

345 X-ray photoelectron spectroscopy (XPS) with an Al Kα source was conducted using a Thermo Scientific K-Alpha

346   instrument, and Shirley background subtraction was employed for data analysis. Attenuated total reflection Fourier-

347   transform infrared spectroscopy (ATR-FTIR) was performed on a Bruker Vertex80 FTIR instrument.

348

349   *Data availability*

        All data is available from the authors upon reasonable request.

370   **Authors Contributions**

371   Y.S., X.Z., and M.F.G. designed this project under the guidance of M.S. and P.Y. Y.S. synthesized the material and

372   conducted electrochemical and electron microscopy characterization with the help of S.C., S.Y, I.R., H.C. and V.A. Y.S.

373   and X.Z. performed the nano-FTIR experiment and analyzed the data, which was assisted by S.C. and H.B. M.F.G.

374   conducted Raman measurements. A.J. and J.Q. performed DFT calculations. SFG measurements were conducted by

375   K.N and X.Z. All the authors contributed to the discussion of the experiment results and preparation of the manuscript.

Competing Interests

The authors declare no competing interests.

References

1   Chen, G., Roy, I., Yang, C. & Prasad, P. N. Nanochemistry and Nanomedicine for Nanoparticle-based Diagnostics and Therapy. *Chem. Rev.* **116**, 2826-2885 (2016).

2   Mura, S., Nicolas, J. & Couvreur, P. Stimuli-responsive nanocarriers for drug delivery. *Nat. Mater* **12**, 991-1003 (2013).

3   Owen, J. The coordination chemistry of nanocrystal surfaces. *Science* **347**, 615-616 (2015).

4   Kelly, K. L., Coronado, E., Zhao, L. L. & Schatz, G. C. The Optical Properties of Metal Nanoparticles: The Influence of Size, Shape, and Dielectric Environment. *J. Phys. Chem. B* **107**, 668-677 (2003).

5   Guntern, Y. T. *et al.* Colloidal Nanocrystals as Electrocatalysts with Tunable Activity and Selectivity. *ACS Catal.* **11**, 1248-1295 (2021).

6   Xie, C., Niu, Z., Kim, D., Li, M. & Yang, P. Surface and Interface Control in Nanoparticle Catalysis. *Chem. Rev.* **120**, 1184-1249 (2020).

7   Puntes, V. F., Krishnan, K. M. & Alivisatos, A. P. Colloidal Nanocrystal Shape and Size Control: The Case of Cobalt. *Science* **291**, 2115-2117 (2001).

8   Sun, Y. & Xia, Y. Shape-Controlled Synthesis of Gold and Silver Nanoparticles. *Science* **298**, 2176-2179 (2002).

9   Le Goas, M. *et al.* (In)stability of ligands at the surface of inorganic nanoparticles: A forgotten question in nanomedicine? *Nano Today* **45**, 101516 (2022).

10   Heuer-Jungemann, A. *et al.* The Role of Ligands in the Chemical Synthesis and Applications of Inorganic Nanoparticles. *Chem. Rev.* **119**, 4819-4880 (2019).

11   Rossi, L. M., Fiorio, J. L., Garcia, M. A. S. & Ferraz, C. P. The role and fate of capping ligands in colloidally prepared metal nanoparticle catalysts. *Dalton Trans.* **47**, 5889-5915 (2018).

12   Dabbagh, A. *et al.* Polyethylene glycol-coated porous magnetic nanoparticles for targeted delivery of chemotherapeutics under magnetic hyperthermia condition. *Int. J. Hyperth.* **36**, 104-114 (2019).

13   Le Goas, M. *et al.* Irradiation Effects on Polymer-Grafted Gold Nanoparticles for Cancer Therapy. *ACS Appl. Bio Mater.* **2**, 144-154 (2019).

14   Yan, B. *et al.* Characterization of surface ligands on functionalized magnetic nanoparticles using laser desorption/ionization mass spectrometry (LDI-MS). *Nanoscale* **5**, 5063-5066 (2013).

15   Yu, D., Wehrenberg, B. L., Jha, P., Ma, J. & Guyot-Sionnest, P. Electronic transport of n-type CdSe quantum dot films: Effect of film treatment. *J. Appl. Phys.* **99** (2006).

16   Lu, L., Zou, S. & Fang, B. The Critical Impacts of Ligands on Heterogeneous Nanocatalysis: A Review. *ACS Catal.* **11**, 6020-6058 (2021).

17   Kim, D. *et al.* Selective CO_2 electrocatalysis at the pseudocapacitive nanoparticle/ordered-ligand interlayer. *Nat. Energy* **5**, 1032-1042 (2020).

18   Yu, S. *et al.* Nanoparticle Assembly Induced Ligand Interactions for Enhanced Electrocatalytic CO_2 Conversion. *J. Am. Chem. Soc.* **143**, 19919-19927 (2021).

19   Yu, S., Louisia, S. & Yang, P. The Interactive Dynamics of Nanocatalyst Structure and Microenvironment during Electrochemical CO2 Conversion. *JACS Au* **2**, 562-572 (2022).

20   Yang, Y. *et al.* Operando studies reveal active Cu nanograins for CO_2 electroreduction. *Nature* **614**, 262-269 (2023).

21   Bechtel, H. A., Johnson, S. C., Khatib, O., Muller, E. A. & Raschke, M. B. Synchrotron infrared nano-spectroscopy and -imaging. *Surf. Sci. Rep.* **75**, 100493 (2020).

22   Wu, C.-Y. *et al.* High-spatial-resolution mapping of catalytic reactions on single particles. *Nature* **541**, 511-515 (2017).

23   Bechtel, H. A., Muller, E. A., Olmon, R. L., Martin, M. C. & Raschke, M. B. Ultrabroadband infrared nanospectroscopic imaging. *Proc. Natl Acad. Sci. USA* **111**, 7191-7196 (2014).

24   Muller, E. A., Pollard, B., Bechtel, H. A., Van Blerkom, P. & Raschke, M. B. Infrared vibrational nano-crystallography and nano-imaging. *Sci. Adv.* **2** (2016).

25   Amenabar, I. *et al.* Structural analysis and mapping of individual protein complexes by infrared nanospectroscopy. *Nat. Commun.* **4** (2013).

26   Zhao, X. *et al. In vitro* investigation of protein assembly by combined microscopy and infrared spectroscopy at the nanometer scale. *Proc. Natl Acad. Sci. USA* **119**, e2200019119 (2022).

27   Lu, Y.-H. *et al.* Ultrathin Free-Standing Oxide Membranes for Electron and Photon Spectroscopy Studies of Solid–Gas and Solid–Liquid Interfaces. *Nano Lett.* **20**, 6364-6371 (2020).

28   Lu, Y.-H. *et al.* Infrared Nanospectroscopy at the Graphene–Electrolyte Interface. *Nano Lett.* **19**, 5388-5393 (2019).

29   He, X., Larson, J. M., Bechtel, H. A. & Kostecki, R. In situ infrared nanospectroscopy of the local processes at the Li/polymer electrolyte interface. *Nat. Commun.* **13**, 1398 (2022).

30   Zenobi, M. C., Luengo, C. V., Avena, M. J. & Rueda, E. H. An ATR-FTIR study of different phosphonic acids in aqueous solution. *Spectrochim Acta A Mol Biomol Spectrosc* **70**, 270-276 (2008).

31   Luschtinetz, R., Seifert, G., Jaehne, E. & Adler, H.-J. P. Infrared Spectra of Alkylphosphonic Acid Bound to Aluminium Surfaces. *Macromol. Symp.* **254**, 248-253 (2007).

32   Geldof, D. *et al.* Binding modes of phosphonic acid derivatives adsorbed on TiO_2 surfaces: Assignments of experimental IR and NMR spectra based on DFT/PBC calculations. *Surf. Sci.* **655**, 31-38 (2017).

33   Lee, J. T., Hati, S., Fahey, M. M., Zaleski, J. M. & Sardar, R. Surface-Ligand-Controlled Enhancement of Carrier Density in Plasmonic Tungsten Oxide Nanocrystals: Spectroscopic Observation of Trap-State Passivation via Multidentate Metal Phosphonate Bonding. *Chem. Mater.* **34**, 3053-3066 (2022).

34   Klähn, M. *et al.* IR Spectra of Phosphate Ions in Aqueous Solution: Predictions of a DFT/MM Approach Compared with Observations. *J. Phys. Chem. A* **108**, 6186-6194 (2004).

35   Skibinski, E. S., DeBenedetti, W. J. I. & Hines, M. A. Solution Deposition of Phenylphosphinic Acid Leads to Highly Ordered, Covalently Bound Monolayers on TiO_2 (110) Without Annealing. *J. Phys. Chem. C* **121**, 14213-14221 (2017).

36   Egerton, R. F. Radiation damage to organic and inorganic specimens in the TEM. *Micron* **119**, 72-87 (2019).

37   Leijten, Z. J. W. A., Keizer, A. D. A., de With, G. & Friedrich, H. Quantitative Analysis of Electron Beam Damage in Organic Thin Films. *J. Phys. Chem. C* **121**, 10552-10561 (2017).

38   Lackey, H. E., Nelson, G. L., Lines, A. M. & Bryan, S. A. Reimagining pH Measurement: Utilizing Raman Spectroscopy for Enhanced Accuracy in Phosphoric Acid Systems. *Anal. Chem.* **92**, 5882-5889 (2020).

39   Belding, L. *et al.* Conformation, and Charge Tunneling through Molecules in SAMs. *J. Am. Chem. Soc.* **143**, 3481-3493 (2021).

40   Bodo, E. *et al.* Interaction of a long alkyl chain protic ionic liquid and water. *Chem. Phys.* **140** (2014).

41   Lütgens, M., Chatzipapadopoulos, S. & Lochbrunner, S. Ultrafast CARS with Improved Spectral Resolution. *EPJ Web Conf* **41**, 05007 (2013).

42   Shan, W., Liu, R., Zhao, H. & Liu, J. Bicarbonate Rebalances the *COOH/*OCO⁻ Dual Pathways in CO_2 Electrocatalytic Reduction: In Situ Surface-Enhanced Raman Spectroscopic Evidence. *J. Phys. Chem. Lett.* **13**, 7296-7305 (2022).

43   Goldie, S. J., Bush, S., Cumming, J. A. & Coleman, K. S. A Statistical Approach to Raman Analysis of Graphene-Related Materials: Implications for Quality Control. *ACS Appl. Nano Mater.* **3**, 11229-11239 (2020).

44   Monteiro, M. C. O. *et al.* Absence of CO_2 electroreduction on copper, gold and silver electrodes without metal cations in solution. *Nat. Catal* **4**, 654-662 (2021).

45   Shin, S.-J. *et al.* A unifying mechanism for cation effect modulating C1 and C2 productions from CO_2 electroreduction. *Nat. Commun.* **13**, 5482 (2022).

46   Wijesuriya, S., Burugapalli, K., Mackay, R., Ajaezi, G. C. & Balachandran, W. Chemically Roughened Solid Silver: A Simple, Robust and Broadband SERS Substrate. *Sens.* **16**, 1742 (2016).

47   Kresse, G. & Hafner, J. Ab initio molecular dynamics for liquid metals. *Phys. Rev. B Condens. Matter* **47**, 558-561 (1993).

48   Kresse, G. & Furthmüller, J. Efficiency of ab-initio total energy calculations for metals and semiconductors using a plane-wave basis set. *Comput. Mater. Sci.* **6**, 15-50 (1996).

49   Kresse, G. & Furthmüller, J. Efficient iterative schemes for ab initio total-energy calculations using a plane-wave basis set. *Phys. Rev. B Condens. Matter* **54**, 11169-11186 (1996).

50   Kresse, G. & Joubert, D. From ultrasoft pseudopotentials to the projector augmented-wave method. *Phys. Rev. B Condens. Matter* **59**, 1758-1775 (1999).

51   Perdew, J. P., Burke, K. & Ernzerhof, M. Generalized Gradient Approximation Made Simple. *Phys. Rev. Lett.* **77**, 3865-3868 (1996).

52   Grimme, S., Antony, J., Ehrlich, S. & Krieg, H. A consistent and accurate ab initio parametrization of density functional dispersion correction (DFT-D) for the 94 elements H-Pu. *Chem. Phys.* **132** (2010).

53   Wang, Y., Wang, W., Fan, K.-N. & Deng, J. Structural and electronic properties of silver surfaces: ab initio pseudopotential density functional study. *Surf. Sci.* **490**, 125-132 (2001).

54   Yang, S. *et al.* Chloride-Assisted Corrosion of Copper and Protection by Benzotriazole. *ACS Appl. Mater. Interfaces.* **14**, 6093-6101 (2022).